

Synthesis of BiOBr, Bi₃O₄Br, and Bi₁₂O₁₇Br₂ by controlled hydrothermal method and their photocatalytic properties



Kun-Lin Li ^a, Wenlian William Lee ^{b,c}, Chung-Shin Lu ^d, Yong-Ming Dai ^a, Shang-Yi Chou ^a, Hong-Lin Chen ^a, Ho-Pan Lin ^a, Chiing-Chang Chen ^{a,*}

^a Department of Science Application and Dissemination, National Taichung University of Education, Taichung 403, Taiwan

^b Department of Occupational Safety and Health, Chung-Shan Medical University, Taichung 402, Taiwan

^c Department of Occupational Medicine, Chung Shan Medical University Hospital, Taichung 402, Taiwan

^d Department of General Education, National Taichung University of Science and Technology, Taichung 404, Taiwan

ARTICLE INFO

Article history:

Received 22 September 2013

Received in revised form 6 March 2014

Accepted 12 April 2014

Available online 13 May 2014

Keywords:

Photocatalytic

BiOBr

Bi₃O₄Br

Bi₁₂O₁₇Br₂

Hydrothermal

Crystal violet

ABSTRACT

Bismuth oxybromides have received remarkable attention in recent years because of their stability, suitable band gaps, and relatively superior photocatalytic abilities. In the preparation procedure, BiBr₃ is dissolved in an aqueous solution, NaOH aqueous solution is added to adjust the pH value, and then the aqueous solution is transferred into a 30 mL Teflon-lined autoclave, which is heated to 100–250 °C for 4, 6, and 12 h and then naturally cooled to room temperature. The composition and morphologies of bismuth oxybromides could be controlled by adjusting some growth parameters, including reaction pH, time, and temperature. The products are characterized by XRD, SEM-EDS, HR-TEM, DR-UV, BET, and HR-XPS. It is demonstrated that BiOBr, Bi₃O₄Br, and Bi₁₂O₁₇Br₂ can be selectively prepared through a facile solution-based hydrothermal method. UV-vis spectra show the three materials being the indirect semiconductors with optical bandgaps of 2.85, 2.66, and 2.42 eV. Photocatalytic efficiency of the powder suspension is evaluated by measuring the crystal violet (CV) or salicylic acid (SA) concentration. This is a study to show the superior activities of BiOBr, Bi₃O₄Br, and Bi₁₂O₁₇Br₂ as a promising visible-light-responsive photocatalyst.

© 2014 Taiwan Institute of Chemical Engineers. Published by Elsevier B.V. All rights reserved.

1. Introduction

In the past decade, heterogeneous photocatalysis for environmental remediation and solar energy conversion has aroused extensive interests. An inexpensive photocatalyst and environmentally sturdy is an important component for the practical application of photocatalysis. Among the various photocatalytic materials, nano-scaled TiO₂ is studied mostly; however, it can only be activated by UV irradiation, which contains less than 5% of the solar spectrum [1]. To utilize visible light (43% energy in solar spectrum) and harvest solar energy efficiently, intensive efforts have attempted to develop visible-light-responsive photocatalysts, such as metal/nonmetal modified TiO₂ [2], inorganic bismuth compounds (Bi₂WO₆ [3], Bi₂MoO₆ [4] and BiVO₄ [5]), and ferrites [6]. Although most photocatalysts show markedly visible-light-responsive activities, their stability, rela-

tionship between structure and photocatalytic reactivity, and photocatalysis mechanism remain uncertain [7]. For that reason, synthesizing novel visible-light-responsive photocatalysts and exploring their photocatalysis performance are of great interests and potential award [8].

Bismuth oxyhalides, BiOX (X = I, Br, Cl), belong to the family of main group multi-component metal oxyhalides V–VI–VII, an important class of ternary compounds, which have recently induced great interests because of their uniquely and excellently optical, magnetic, electrical, and photoluminescence properties as well as their potential photocatalytic abilities [9,10]. Among bismuth oxyhalides, BiOBr has received remarkable attention in recent years because of the stability, suitable band gaps, and relatively superior photocatalytic abilities [11–14,8,15–25]. BiOBr flakes show superior photocatalytic abilities than P25 TiO₂ does on degrading dyes under visible light (>400 nm) illumination [11]. The Fang group synthesizes BiOBr by hydrothermal methods, which exhibit excellent photocatalytic efficiency and good stability during the microcystin-LR photodegradation under visible light irradiation [12]. Xu et al. synthesized BiOBr by facile co-precipitation methods, which exhibited excellent photocatalytic

* Corresponding author. Tel.: +886 4 2218 3406; fax: +886 4 2218 3560.

E-mail addresses: ccchen@mail.ntcu.edu.tw, ccchen@ms3.ntcu.edu.tw (C.-C. Chen).

efficiency and good stability during the benzotriazole of photodegradation [10]. In addition, the density functional theory (DFT) calculation showed that the valence-band (VB) top of bismuth oxybromides was composed of hybrid orbitals of Br 4p, O 2p and Bi 6s orbitals, whereas the conduction-band (CB) bottom primarily consisted of Bi 6p orbitals [16]. To infer, bismuth oxybromides with smaller value of Br:O ratio might possibly reduce its VB edge, then show the decrease of the band gap energy (E_g), and present stronger absorption in visible light range than BiOBr [17] did. Although some Br poor bismuth oxybromides, such as $\text{Bi}_{12}\text{O}_{17}\text{Br}_2$ [18], $\text{Bi}_5\text{O}_7\text{Br}$ [19], $\text{Bi}_3\text{O}_4\text{Br}$ [20], $\text{Bi}_{24}\text{O}_{31}\text{Br}_{10}$ [21–23] and $\text{Bi}_4\text{O}_5\text{Br}_2$ [24], have been known to researchers, there is very limited information on their synthesis and optical and photocatalytic properties till now. Very recently, Yu and his coworkers [25] prepared plate-like $\text{Bi}_{24}\text{O}_{31}\text{Br}_{10}$ by calcining flake BiOBr at around 750 °C and investigated its photocatalytic activities for the decomposition of acid orange II. For investigating the photocatalytic properties of Br-poor bismuth oxybromides, Xiao et al. synthesized BiOBr, $\text{Bi}_3\text{O}_4\text{Br}$, $\text{Bi}_{24}\text{O}_{31}\text{Br}_{10}$, and $\text{Bi}_4\text{O}_5\text{Br}_2$ using commercial Bi_2O_3 as the starting material to react with HNO_3 and potassium bromide under hydrothermal conditions [26]. Nevertheless, due to the restriction of crystal growth under routine depositing conditions, the synthesis of Br-poor bismuth oxybromides with nanostructures through wet chemical processes still remains a major challenge, and their potential photocatalytic applications need further investigation as well. The other bismuth oxybromide photocatalyst may be an efficient functional material for the environmental purification of organic pollutants in the aqueous solution. To the best of our knowledge, the comparison of the photocatalytic degradation of organic pollutants by $\text{Bi}_3\text{O}_4\text{Br}$ and $\text{Bi}_{12}\text{O}_{17}\text{Br}_2$ by hydrothermal methods has not been documented in the literature. This study synthesizes BiOBr, $\text{Bi}_3\text{O}_4\text{Br}$, and $\text{Bi}_{12}\text{O}_{17}\text{Br}_2$ and studies their photocatalytic abilities for removing CV in an aqueous solution under visible-light irradiation. The three bismuth oxybromide photocatalysts with high photocatalytic performance are prepared by controlling synthesis conditions; and, the removal efficiency, principal reaction products, and CV degradation pathway using the prepared bismuth oxybromides are also explored.

2. Experiment

2.1. Synthesis of BiOBr, $\text{Bi}_3\text{O}_4\text{Br}$, and $\text{Bi}_{12}\text{O}_{17}\text{Br}_2$

The purchased KBr and Salicylic Acid (SA) from Katayama Chemical Co. and $\text{Bi}(\text{NO}_3)_3 \cdot 5\text{H}_2\text{O}$ and CV dye from Tokyo Kasei Kogyo Co. were obtained and used without any further purification. Reagent-grade nitric acid, sodium hydroxide, ammonium acetate, and HPLC-grade methanol were obtained from Merck. The de-ionized water used in this study was purified with a Milli-Q water ion-exchange system (Millipore Co.) for a resistivity of $1.8 \times 10^7 \Omega \text{ cm}$.

Three millimoles of BiBr_3 was first mixed in a 30 mL flask. With continuous stirring, 2 M NaOH was added dropwise to adjust the pH value to 1–13. The 10 mL solution was then stirred vigorously for 30 min and transferred into a 30 mL Teflon-lined autoclave, which was heated up to 100–250 °C for 4 h and then naturally cooled down to room temperature. The resulting solid product was collected by filtration, washed with deionized water and methanol to remove any possible ionic species in the product, and then dried at 60 °C overnight. The samples are listed in Table 1. A variety of reaction conditions in hydrothermal methods were employed (including pH value, temperatures, and time) as shown the catalyst codes, namely BB-1-110-4 to BB-14-250-4 for as-prepared samples, respectively.

Table 1

Bismuth oxybromides obtained under different reaction pH value, reaction temperature, and reaction time.

pH	Temp (°C)			
	100	150	200	250
1	BB-1-100-4	BB-1-150-4	BB-1-200-4	BB-1-250-4
4	BB-4-100-4	BB-4-150-4	BB-4-200-4	BB-4-250-4
7	BB-7-100-4	BB-7-150-4	BB-7-200-4	BB-7-250-4
10	BB-10-100-4	BB-10-150-4	BB-10-200-4	BB-10-250-4
12	BB-12-100-4	BB-12-150-4	BB-12-200-4	BB-12-250-4
13	BB-13-100-4	BB-13-150-4	BB-13-200-4	BB-13-100-4
14	BB-14-100-4	BB-14-150-4	BB-14-200-4	BB-14-100-4

2.2. Instruments and analytical methods

XRD patterns were recorded on a MAC Sience, MXP18 X-ray diffractometer with $\text{Cu K}\alpha$ radiation, and operated at 40 kV and 80 mA. The field-emission transmission electron microscopy (FE-TEM) images, SAED patterns, high-resolution transmission electron microscopy (HRTEM) images and an energy-dispersive X-ray spectrum (EDS) were taken on a JEOL- 2010 transmission electron microscope with an accelerating voltage of 200 kV. FE-SEM-EDS measurements were carried out with a field-emission microscope (JEOL JSM-7401F) at an acceleration voltage of 15 kV and an HRXPS measurement was carried out with ULVAC-PHI XPS. The $\text{Al K}\alpha$ radiation was generated with a voltage of 15 kV. The BET specific surface areas of the samples were measured with an automatic system (Micromeritics Gemini 237 °C) using nitrogen gas as the adsorbate, at liquid nitrogen temperature. Cryogenic cathodoluminescence (CL) measurements were carried out on JEOL JSM7001F. The HPLC-PDA-ESI-MS system consisted of a Waters 1525 binary pump, a 2998 photodiode array detector, and a 717 plus autosampler. Besides, a ZQ2000 micromass detector and an Atlantis™ dC18 column (250 mm × 4.6 mm i.d., dp = 5 μm) were used for separation and identification. The column effluent was introduced into the ESI source of the mass spectrometer.

2.3. Evaluation of photocatalytic activity

The aqueous suspensions of CV (or SA) (100 mL, 10 ppm) and the amount of catalyst powder were placed in the Pyrex flask. The pH value of the suspension was adjusted by adding either NaOH or HNO_3 solution. Prior to the irradiation, the suspension was magnetically stirred in the dark for ca. 30 min to establish adsorption/desorption equilibrium between the dye and the surface of the catalyst under ambient air-equilibrated conditions. The irradiation was carried out using visible-light lamps (150 W Xe arc). The light intensity was fixed 35.1 W/m^2 when the reactor was placed 30 cm away from the light source. The irradiation experiments of CV (or SA) were carried out on stirred aqueous solution contained in a 100 mL flask. At the given irradiation time intervals, 5 mL aliquot was collected and centrifuged to remove the catalyst. The supernatant was analyzed by UV-vis (HPLC-PDA-MS) after readjusting the chromatographic conditions in order to make the mobile phase compatible with the working conditions of the mass spectrometer.

3. Results and discussion

3.1. Characterization of the BiOBr, $\text{Bi}_3\text{O}_4\text{Br}$, and $\text{Bi}_{12}\text{O}_{17}\text{Br}_2$

Fig. 1 and Figs. S1–S4 of the Supplementary data shows the XRD patterns of the as-prepared samples. All the samples synthesized using the hydrothermal method described at different temperature and pH were BiOBr (JCPDS 01-078-0348), $\text{Bi}_3\text{O}_4\text{Br}$

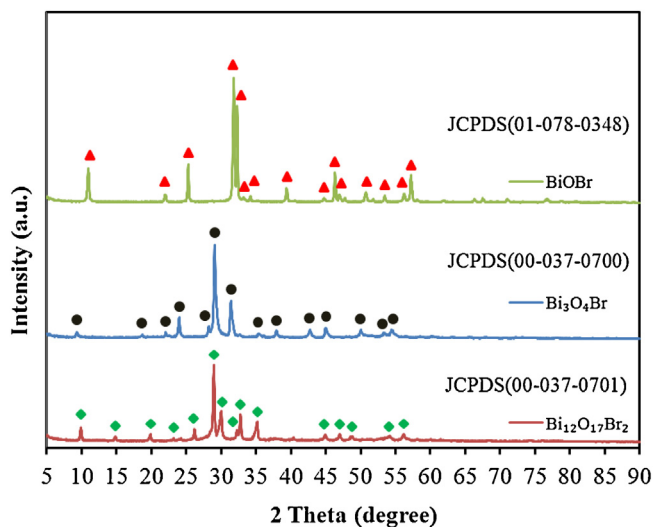
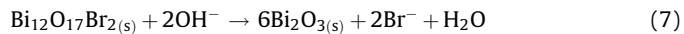
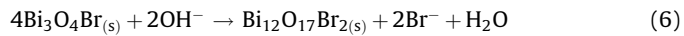
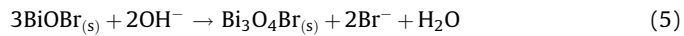
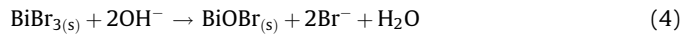
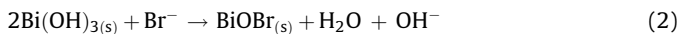


Fig. 1. XRD patterns of BiOBr (BB-4-150-4), Bi₃O₄Br (BB-13-100-4), and Bi₁₂O₁₇Br₂ (BB-13-250-4).

(JCPDS 00-037-0700), Bi₁₂O₁₇Br₂ (JCPDS 00-037-0701), and α-Bi₂O₃ (JCPDS 41-1449) phase. From the results listed in Table 2, the XRD patterns are identical to those reported for Bi₁₂O₁₇Br₂ at pH = 13, temp = 200 and 250 °C, Bi₃O₄Br at pH = 13, temp = 100 and 150 °C, Bi₂O₃ at pH = 14 ad temp = 100–250 °C, and BiOBr for the other conditions, respectively. It was found that, with the increase of hydrothermal temperature range from 100 to 250 °C and hydrothermal pH values from 1 to 14, a gradual change in the crystal phase of the reflection peaks took place, which indicated a formation in the crystal phase from BiOBr, Bi₃O₄Br, and Bi₁₂O₁₇Br₂ to α-Bi₂O₃ at different reaction temperature and pH values. In this experiment, pH and temperature play the key roles in controlling the composition and anisotropic growth of crystals. The results show that a series of changes in the compounds occur at different pH values and reaction temperature, described as BiOBr → Bi₃O₄Br → Bi₁₂O₁₇Br₂ → α-Bi₂O₃. It is demonstrated that bismuth oxybromides can be selectively prepared through adjusted pH values under the hydrothermal method. The possible processes for the formation of bismuth oxybromides are described as follows [Eqs. (1)–(7)]:



These equations showed that BiOBr was formed at the beginning of the reaction and then OH⁻ gradually substituted Br⁻ in the basic conditions, which resulted in the reduced content of Br⁻ in the products. Increasing the pH would gradually obtain Bi₃O₄Br, Bi₁₂O₁₇Br₂, and α-Bi₂O₃. The higher the pH value, the lower the Br⁻ content in the products, until the content of Br⁻ in the products was fully replaced by OH⁻, finally resulting in the formation of α-Bi₂O₃ under strong basic conditions. However, BiOBr was the exclusive product at pH 1–12 and temp 100–250 °C. A competitive relationship typically existed between OH⁻ and Br⁻ ions in the basic solution. By controlling the pH of the reaction, different compositions of bismuth oxybromides were obtained. Besides, different compositions of bismuth oxybromides were also obtained by controlling the reaction temperature.

The surface morphology and the composition of the BiOBr, Bi₃O₄Br, and Bi₁₂O₁₇Br₂ are examined by FE-SEM-EDS (Fig. 2, Figs. S5–S7, and Table 3). From Fig. 2 and Figs. S5–S7, these samples display irregular nanosheet and/or nanoplate shapes with a lateral size of several micrometers and a thickness between 5 and 10 nm. The FE-SEM image showed that the morphology of the bismuth oxybromide samples obtained at different reaction temperature turned from small sheets to irregular sheets, nanoplates, and flower-like crystals, and then became larger plates. Samples exhibited a plate-like irregular shape with a lateral size of several decade micrometers. The EDS results of Table 3 show that the main elements of these samples are bismuth, bromine, and oxygen. The Br atomic ratios (%) of the samples were within the range 29.31–5.21, which corresponded to BiOBr, Bi₃O₄Br, and Bi₁₂O₁₇Br₂, compared to the stoichiometric ratio (Bi:Br = 1, 3, 6), and could be selectively prepared through a facile solution-based hydrothermal method.

Table 3

Physical and chemical properties of bismuth oxybromides samples by prepared under different pH value.

Catalyst code	Catalyst	EDS of atomic ratio (%)			<i>E_g</i> (eV)
		Bi	O	Br	
BB-1-100-4	BiOBr	27.06	47.55	25.39	2.83
BB-4-100-4	BiOBr	29.51	42.89	27.60	2.85
BB-7-100-4	BiOBr	28.37	45.61	26.02	2.85
BB-10-100-4	BiOBr	27.82	46.75	25.43	2.83
BB-13-100-4	Bi ₃ O ₄ Br	36.27	53.30	10.43	2.66
BB-1-150-4	BiOBr	30.23	46.58	23.19	2.85
BB-4-150-4	BiOBr	32.14	38.56	29.31	2.85
BB-7-150-4	BiOBr	29.52	41.97	28.51	2.83
BB-10-150-4	BiOBr	28.34	46.19	25.47	2.86
BB-13-150-4	Bi ₃ O ₄ Br	30.68	59.77	9.55	2.65
BB-1-200-4	BiOBr	26.47	45.99	27.54	2.81
BB-4-200-4	BiOBr	30.21	42.20	27.59	2.83
BB-7-200-4	BiOBr	29.11	45.01	25.88	2.83
BB-10-200-4	BiOBr	29.17	43.85	26.98	2.82
BB-13-200-4	Bi ₁₂ O ₁₇ Br ₂	37.72	56.50	5.78	2.42
BB-1-250-4	BiOBr	28.62	42.48	28.90	2.77
BB-4-250-4	BiOBr	33.49	36.87	29.63	2.78
BB-7-250-4	BiOBr	29.49	45.07	25.45	2.80
BB-10-250-4	BiOBr	31.77	40.82	28.34	2.81
BB-13-250-4	Bi ₁₂ O ₁₇ Br ₂	35.38	59.41	5.21	2.42

Table 2
Crystalline phase changes of bismuth oxybromides prepared under different pH value and temperature. (● BiOBr; ▲ Bi₃O₄Br; ■ Bi₁₂O₁₇Br₂; ◆ Bi₂O₃).

pH	Temp (°C)			
	100	150	200	250
1	●			
4	●	●		
7	●	●	●	
10	●	●	●	●
12	●	●		
13	◆	▲	■	
14	◆	◆	◆	◆

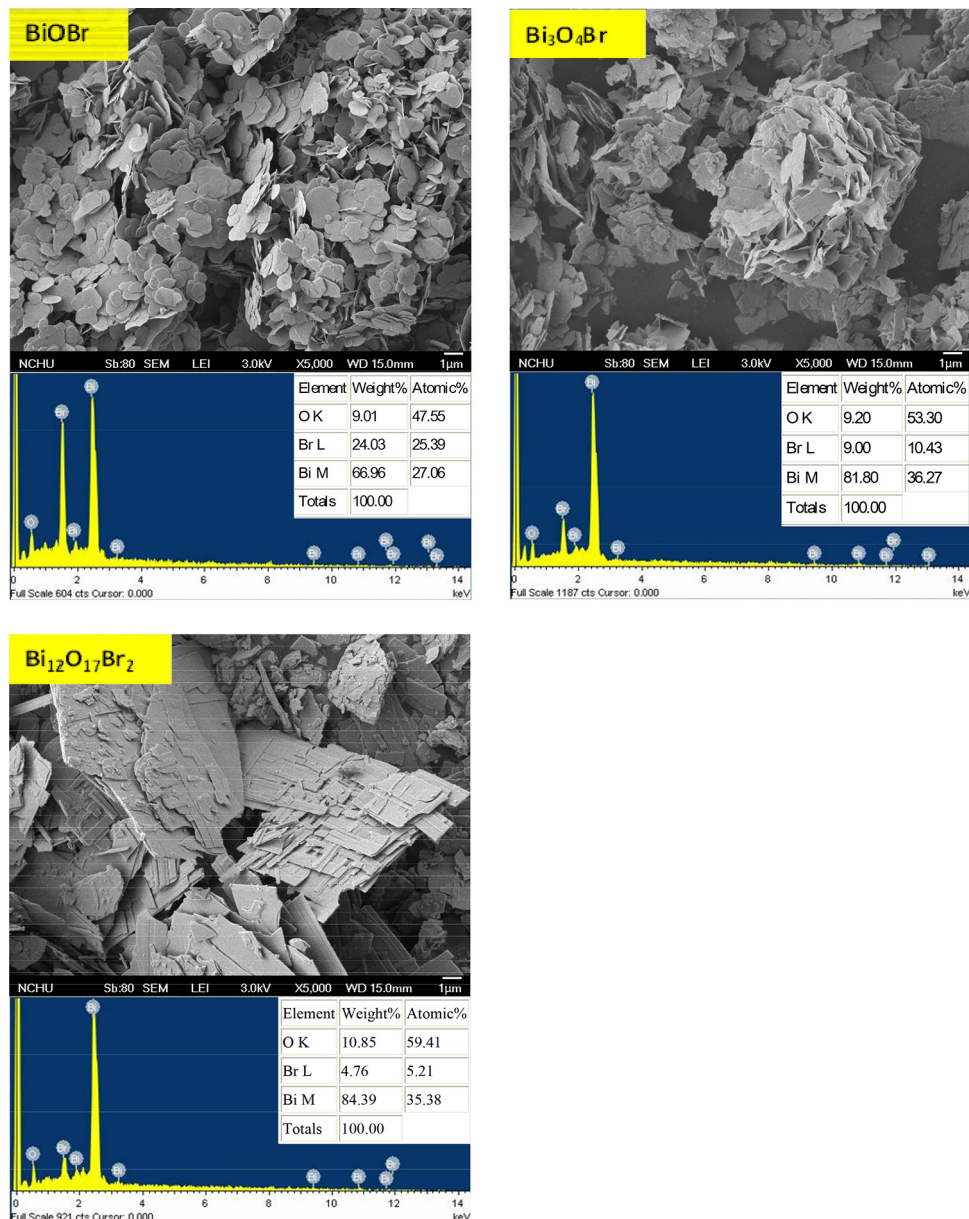


Fig. 2. SEM images and EDS of BiOBr, Bi₃O₄Br, and Bi₁₂O₁₇Br₂ prepared by the hydrothermal autoclave method at different pH values.

Fig. 3 displays that BiOBr, Bi₃O₄Br, and Bi₁₂O₁₇Br₂ are composed of flakes with different sizes, consistent with the TEM observation. The HR-TEM image reveals that one set of different lattice images was found with the *d* spacing of 0.280, 0.284, and 0.283 nm, corresponding to the (0 0 2) plane of Bi₃O₄Br, the (0 1 2) plane of BiOBr, and the (1 1 9) plane of Bi₁₂O₁₇Br₂, respectively, which was in good accordance with the results of the XRD patterns. The results suggest that Bi₃O₄Br, BiOBr, and Bi₁₂O₁₇Br₂ have been formed in the pure nanosheet or nanoplates materials, which will favor for the separation of photoinduced carriers and thus acquire high photocatalytic activities. In addition, the EDS spectrum shows that the sample includes Bi, O and Br elements. The Bi/Br atomic ratios of the samples are 1.18, 4.36, and 7.99, corresponding to BiOBr, Bi₃O₄Br, and Bi₁₂O₁₇Br₂, respectively.

XPS is employed to examining the purity of the prepared bismuth oxybromide products, and the spectra are shown in **Fig. 4**. According to **Fig. 4(a)**, the observation of transition peaks involving in the Bi 4f,

Br 3d, O 1s, and C 1s orbitals revealed that the catalysts were constituted by the elements of Bi, O, Br, and C. The characteristic binding energy of 158.7–159.4 eV for Bi 4f_{7/2} (**Fig. 4(b)**) reveals a trivalent oxidation state for Bi–O bonding. An additional spin-orbit doublet with the binding energy of 156.1–56.5 eV for Bi 4f_{7/2} is also observed in all samples, suggesting that certain parts of bismuth exist in the Bi–Br bonding [20]. A similar chemical shift of approximately 2.2–2.6 eV for Bi 4f_{7/2} was also observed by Jovalekic et al. [27] and Chen et al. [28,29]. They concluded that the Bi^(+3-x) formal oxidation state could most probably attribute to the substoichiometric forms of Bi within the Bi₂O₂ layer, and the formation of the low oxidation state resulted in oxygen vacancy in the crystal lattice. However, it was assumed that the Bi^(+3-x) formal oxidation state could most likely attribute to the substoichiometric forms of Bi at the outer site of the particles, and the formation of the low oxidation state resulted in oxygen vacancy in the crystal surface. **Fig. 4(c)** shows the high-resolution XPS spectra for the O 1s region,

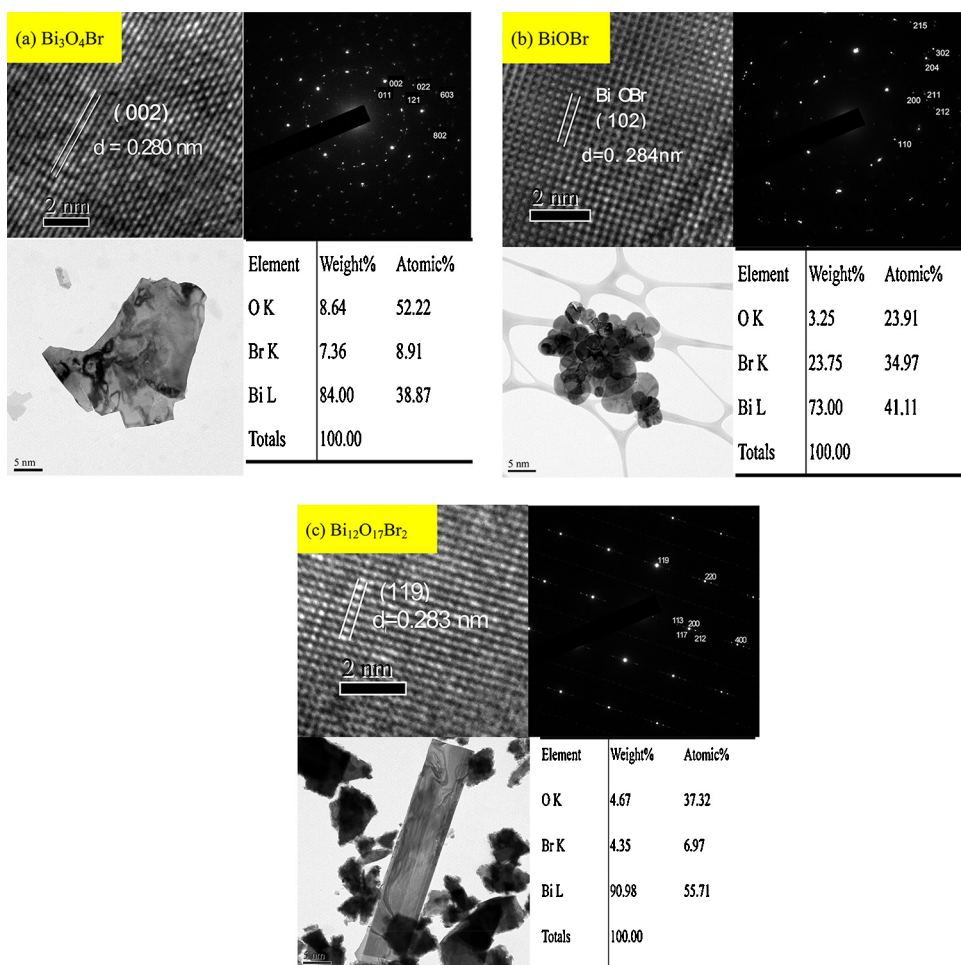


Fig. 3. FE-TEM and HRTEM images, SAED, and EDS of the (a) $\text{Bi}_3\text{O}_4\text{Br}$, (b) BiOBr , and (c) $\text{Bi}_{12}\text{O}_{17}\text{Br}_2$ prepared by the hydrothermal autoclave method.

which could be fitted into two peaks. The main peak at 529.9 eV was attributed to the Bi–O bonds in $(\text{Bi}_2\text{O}_2)^{2+}$ slabs of BiOX layered structure, and the peak at 531.8 eV was assigned to the hydroxyl groups on the surface [30]. The binding energy of 67.8–68.3 eV and 68.7–69.2 eV was referred to Br $3d_{5/2}$ and $3d_{3/2}$ respectively which could be assigned to Br at the monovalent oxidation state (Fig. 4(d)). In the samples, only two strong peaks centered at 163.9 and 158.2 eV could attribute to Bi $4f_{5/2}$ and Bi $4f_{7/2}$, demonstrating that the main chemical states of the bismuth element in the samples were trivalent. The characteristic binding energy of 158.2 eV for Bi $4f_{7/2}$ revealed a trivalent oxidation state for $\text{Bi}^{+3}\text{–O}$ bonding. Two additional spin-orbit doublets with the binding energy of 158.8 and 159.2 eV for Bi $4f_{7/2}$ were also observed in all samples, suggesting that certain parts of bismuth existed in the Bi–Br bonding [20]. The XPS result revealed the possible processes for the formation of bismuth oxybromides described as Eqs. (1)–(7), which were consistent with the previous results by XRD and TEM analyses. The compositions show that the main elements of these samples are

bismuth, bromine, and oxygen in Table 4. The Bi/Br atomic ratios of the samples are 1.82, 4.72, and 7.79, corresponding to BiOBr , $\text{Bi}_3\text{O}_4\text{Br}$ and $\text{Bi}_{12}\text{O}_{17}\text{Br}_2$, respectively. The Bi/Br atomic ratios of the samples corresponded to BiOBr , $\text{Bi}_3\text{O}_4\text{Br}$, and $\text{Bi}_{12}\text{O}_{17}\text{Br}_2$, compared to the stoichiometric ratio ($\text{Bi:Br} = 1, 3, 6$), and could be selectively prepared through a facile solution-based hydrothermal method.

3.2. Optical absorption properties

UV-vis diffuse reflectance spectra of BiOBr , $\text{Bi}_3\text{O}_4\text{Br}$, and $\text{Bi}_{12}\text{O}_{17}\text{Br}_2$ are shown in Fig. 5. The E_g of BiOBr , $\text{Bi}_3\text{O}_4\text{Br}$, and $\text{Bi}_{12}\text{O}_{17}\text{Br}_2$ is determined from a plot of $(\alpha h\nu)^{1/2}$ vs energy ($h\nu$) and elicited to be 2.85, 2.66, and 2.42 eV in Table 3, respectively. It could be observed that BiOBr absorbed visible light slightly while the absorption edge of $\text{Bi}_{12}\text{O}_{17}\text{Br}_2$ extended nearly to the whole spectra of visible light. Moreover, the absorption edges of BiOBr had a monotonic red shift response of $\text{Bi}_{12}\text{O}_{17}\text{Br}_2$.

3.3. BET surface areas and pore structure

Fig. 6 shows the nitrogen adsorption–desorption isotherm curves of BiOBr , $\text{Bi}_3\text{O}_4\text{Br}$, and $\text{Bi}_{12}\text{O}_{17}\text{Br}_2$. The isotherm is close to Type IV (BDDT classification) with a hysteresis loop at highly relative pressure between 0.6 and 1.0 [31]. The shapes of the hysteresis loop is close to Type H3, suggesting the existence of slit-like pores that are generally formed by the aggregation of plate-like particles, which is consistent with the self assembled nanoplate-like morphology of samples [31].

Table 4

Composition and characterization of BiOBr , $\text{Bi}_3\text{O}_4\text{Br}$, and $\text{Bi}_{12}\text{O}_{17}\text{Br}_2$.

Catalyst code	Catalyst	XPS of atomic ratio (%)			BET (m ² /g)	Pore size (Å)	Pore volume (cm ³ /g)
		Bi	O	Br			
BB-4-150-4	BiOBr	44.6	31.0	24.5	7.53	605.60	0.123
BB-13-100-4	$\text{Bi}_3\text{O}_4\text{Br}$	44.4	46.3	9.4	8.58	648.90	0.151
BB-13-250-4	$\text{Bi}_{12}\text{O}_{17}\text{Br}_2$	41.3	53.5	5.3	3.25	493.47	0.042

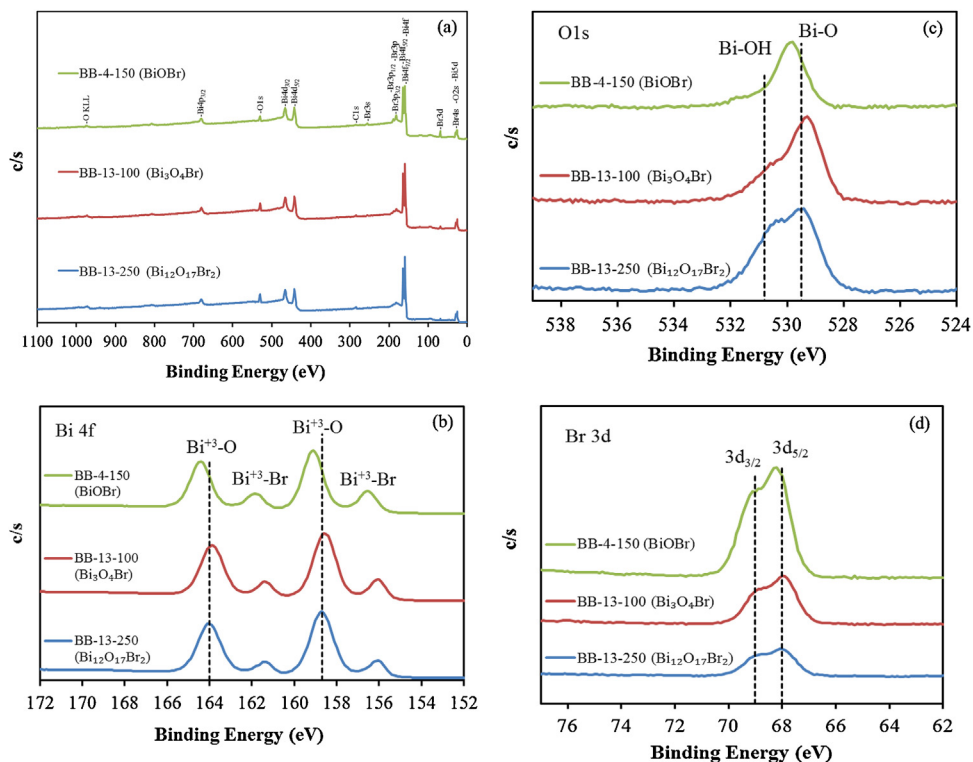


Fig. 4. High resolution XPS spectra of BiOBr, $\text{Bi}_3\text{O}_4\text{Br}$, and $\text{Bi}_{12}\text{O}_{17}\text{Br}_2$.

From Table 4, The BET of the BiOBr, $\text{Bi}_3\text{O}_4\text{Br}$, and $\text{Bi}_{12}\text{O}_{17}\text{Br}_2$ are about 7.53, 8.58, and $3.25 \text{ m}^2/\text{g}$, respectively, which is lower than that of P25-TiO₂ with BET of $55.4 \text{ m}^2/\text{g}$ due to the increased particle size. This nanosheet and nanoplate structure can provide efficient transport paths for reactants and more active sites for the photocatalytic reaction. The structure is also favorable to efficient photo-energy harvesting and introducing the separation of electron-hole pairs, thus promoting the photocatalytic activities.

In Table 4, the pore volumes and sizes of BiOBr, $\text{Bi}_3\text{O}_4\text{Br}$, and $\text{Bi}_{12}\text{O}_{17}\text{Br}_2$ were distributed to $0.123\text{--}0.042 \text{ cm}^3/\text{g}$ and $605.60\text{--}493.7 \text{ \AA}$. A greater specific surface area and pore volume of photocatalyst could supply more surface active sites and

make reactants transport easier, leading to an enhancement of the photocatalytic performance [32]. $\text{Bi}_3\text{O}_4\text{Br}$ had larger BET and pore volume. Thus, the large BET and pore volume of $\text{Bi}_3\text{O}_4\text{Br}$ might play a role in enhancing the photocatalytic activity. These nanosheet and nanoplate structures could provide efficient transport paths for reactants and more active sites for the photocatalytic reaction. The structures were also favorable to efficient photo-energy harvesting and introducing the separation of electron-hole pairs, thus promoting the photocatalytic activity.

3.4. Photocatalytic activity

The photocatalytic performance of BiOBr, $\text{Bi}_3\text{O}_4\text{Br}$, and $\text{Bi}_{12}\text{O}_{17}\text{Br}_2$ catalysts is evaluated by degrading CV under visible light irradiation with 0.5 g/L of catalyst added. The degradation

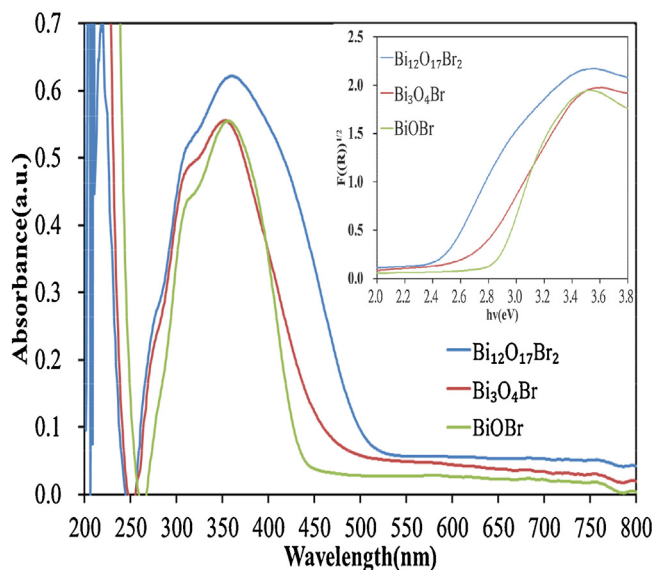


Fig. 5. UV-vis absorption spectra of BiOBr, $\text{Bi}_3\text{O}_4\text{Br}$, and $\text{Bi}_{12}\text{O}_{17}\text{Br}_2$.

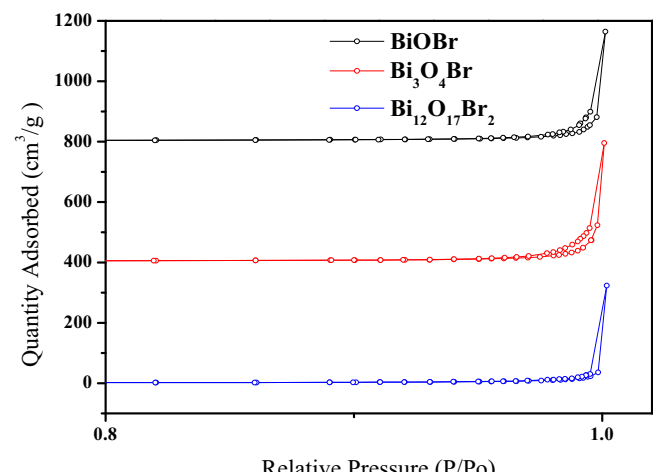


Fig. 6. N_2 adsorption–desorption isotherm distribution curves for BiOBr, $\text{Bi}_3\text{O}_4\text{Br}$, and $\text{Bi}_{12}\text{O}_{17}\text{Br}_2$.

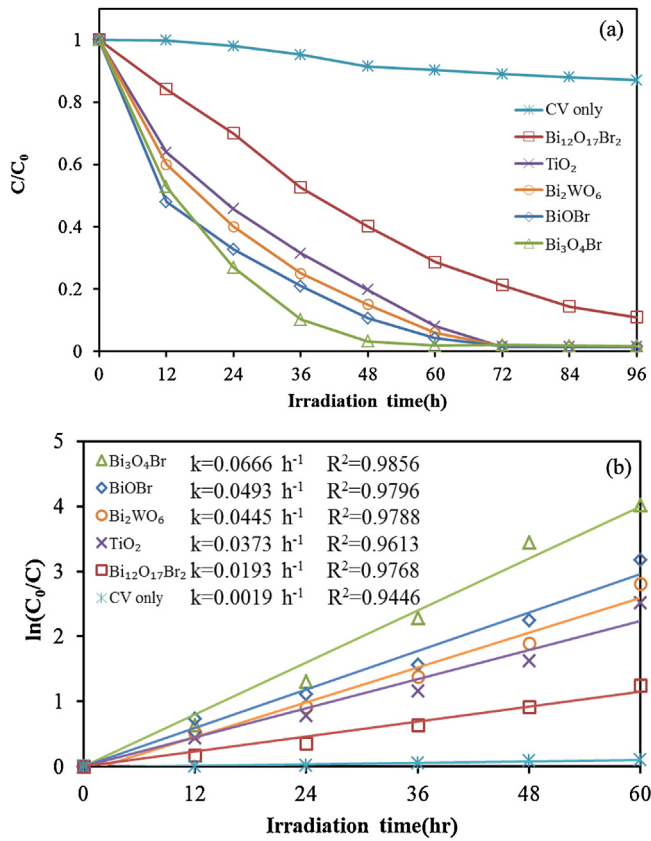


Fig. 7. Photodegradation of CV as a function of irradiation time over different BiOBr, $\text{Bi}_3\text{O}_4\text{Br}$, and $\text{Bi}_{12}\text{O}_{17}\text{Br}_2$ photocatalysts.

efficiency as a function of reaction time is illustrated in Fig. 7. In the absence of catalysts, CV could not be degraded under visible light irradiation. The removal efficiency is enhanced significantly in the presence of photocatalysts. After 72 h irradiation, BiOBr and $\text{Bi}_3\text{O}_4\text{Br}$ show superior photocatalytic performance, with CV removal efficiency up to 99%. In the absence of catalysts, CV could not be degraded under visible light irradiation. The removal efficiency was enhanced significantly in the presence of bismuth oxybromide catalysts. After 60 h irradiation, $\text{Bi}_3\text{O}_4\text{Br}$ showed superior photocatalytic performance, with CV removal efficiency up to 99.9%. The activity of $\text{Bi}_3\text{O}_4\text{Br}$ was higher than those of BiOBr , Bi_2WO_6 , P25- TiO_2 , and $\text{Bi}_{12}\text{O}_{17}\text{Br}_2$. To further understand the reaction kinetics of CV degradation, the apparent pseudo-first-order model [33], expressed by the equation $\ln(C_0/C) = kt$,

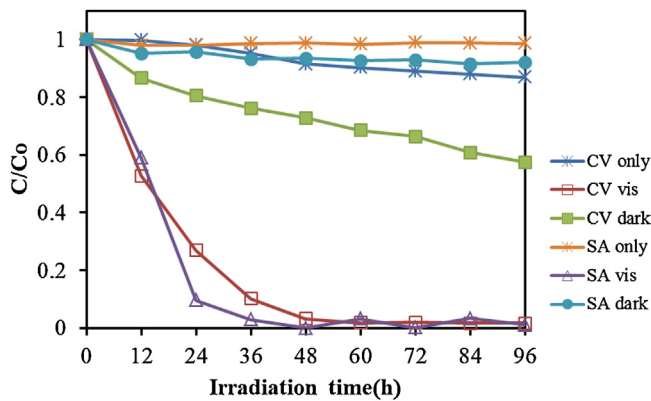


Fig. 8. The photocatalytic activity of $\text{Bi}_3\text{O}_4\text{Br}$ under visible-light irradiation. (0.01 g/L CV; 0.01 g/L SA; 0.05 g/L $\text{Bi}_3\text{O}_4\text{Br}$).

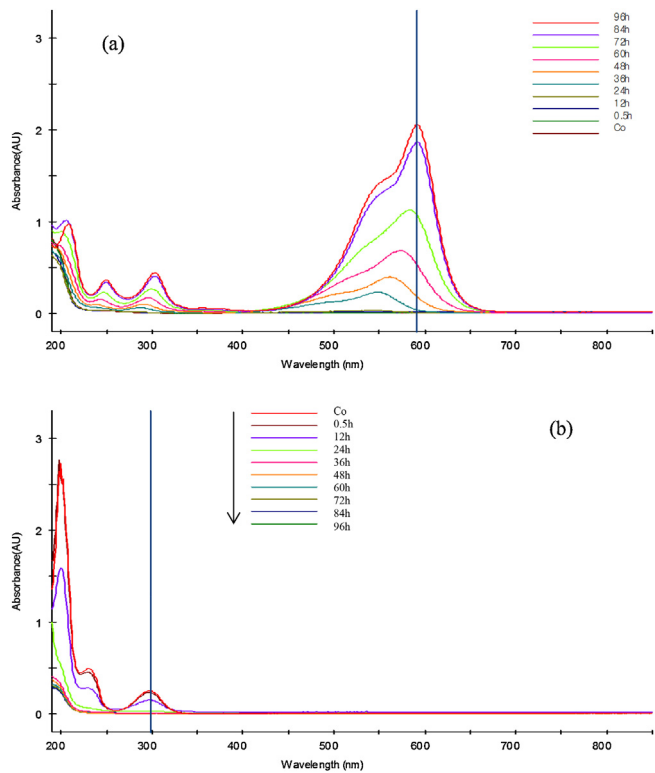


Fig. 9. Temporal UV-vis adsorption spectral changes during the photocatalytic degradation of (a) CV and (b) SA over aqueous $\text{Bi}_3\text{O}_4\text{Br}$ under visible light irradiation.

was applied to the experiments, where k was the apparent pseudo-first-order rate constant (h^{-1}), C the CV concentration in aqueous solution at time t (mg/L), and C_0 the initial CV concentration (mg/L). $\text{Bi}_3\text{O}_4\text{Br}$ was obtained at the maximal degradation rate of $6.66 \times 10^{-2} \text{ h}^{-1}$, greatly higher than the other (Fig. 7(b)). However, this result displayed that $\text{Bi}_3\text{O}_4\text{Br}$ with the highest BET and pore volume represented the highest photocatalytic activity among the samples, which suggested that the changes in the photocatalytic activity was resulted from BET and pore volume. The superior photocatalytic abilities of BiOBr and $\text{Bi}_3\text{O}_4\text{Br}$ may be ascribed to its efficient utilization of visible light and the high separation efficiency of the electron–hole pairs with its hierarchical structure.

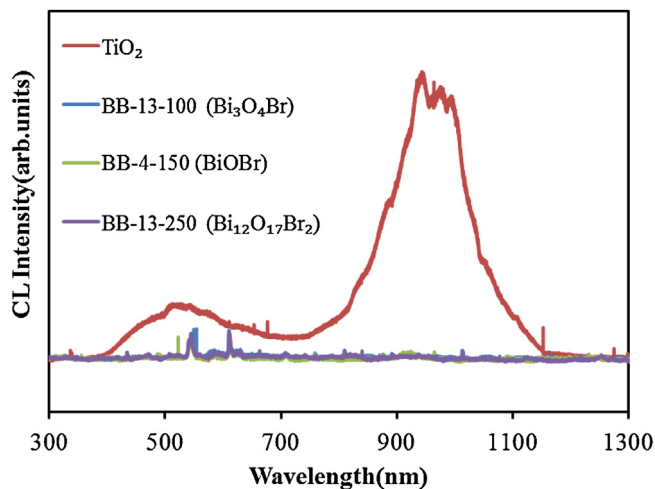


Fig. 10. Cathodoluminescence spectra of TiO_2 , BiOBr , $\text{Bi}_3\text{O}_4\text{Br}$, and $\text{Bi}_{12}\text{O}_{17}\text{Br}_2$.

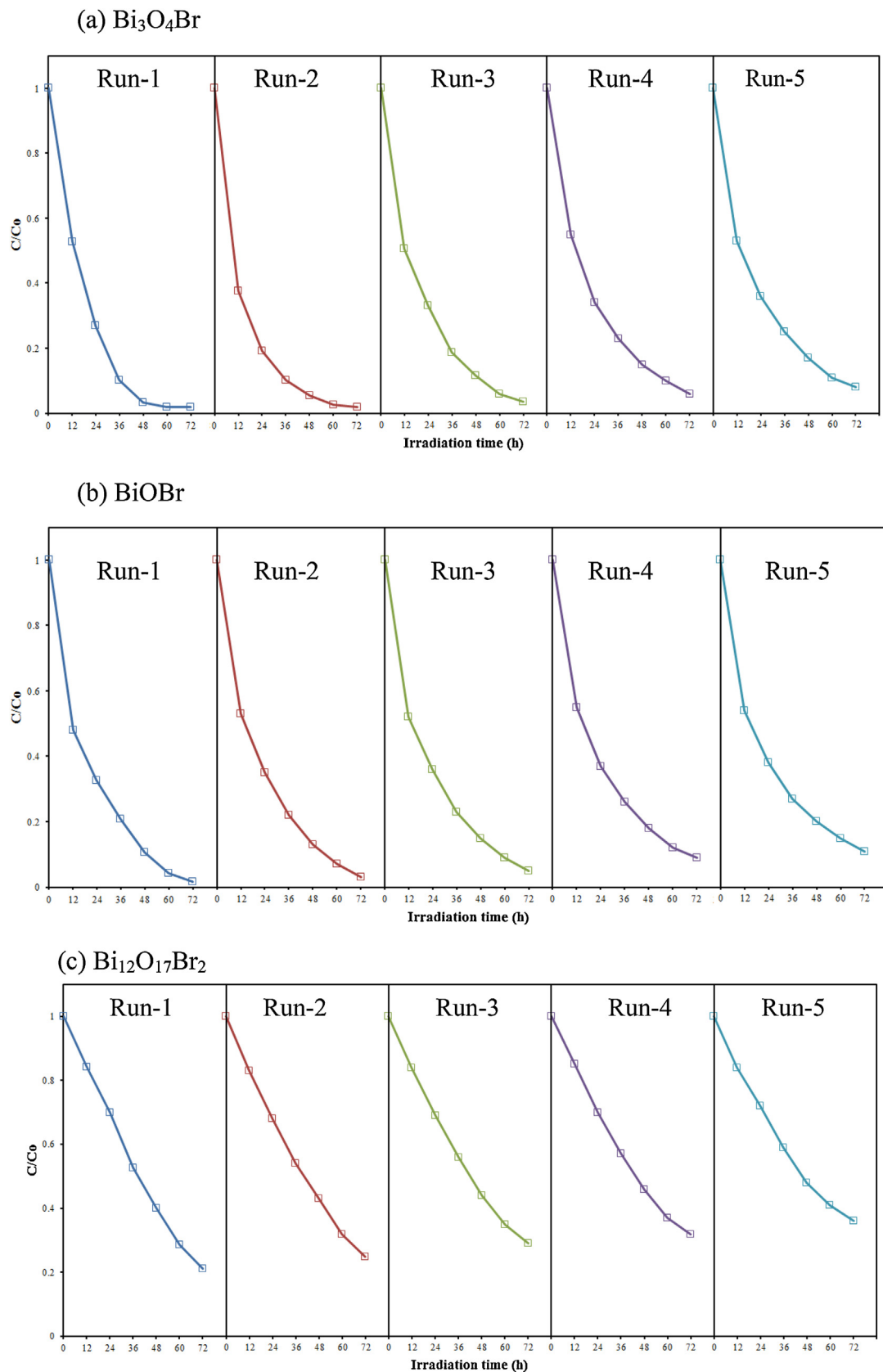


Fig. 11. Cycling runs in the photocatalytic degradation of CV in the presence of (a) $\text{Bi}_3\text{O}_4\text{Br}$, (b) BiOBr , (c) $\text{Bi}_{12}\text{O}_{17}\text{Br}_2$.

The photodegradation rate of the SA using $\text{Bi}_3\text{O}_4\text{Br}$ was found to decrease with the increase of reaction time (Fig. 8). The adsorption resulted in a decrease of about 7.1% in the SA concentration after 96 h, and a decrease in the photocatalytic efficiencies of 98.5% under visible light irradiation in the SA concentration being decomposed after 48 h, respectively.

The changes in the UV-vis spectra during the photodegradation of CV and SA in aqueous dispersions of $\text{Bi}_3\text{O}_4\text{Br}$ under visible-light irradiation are illustrated in Fig. 9. After visible-light irradiation for 60 h, ca. 99.5% of CV was decomposed in Fig. 9(a); after UV irradiation for 36 h, ca. 99.9% of SA degraded in Fig. 9(b). During visible-light irradiation, the characteristic absorption band of the CV dye at 588.3 nm decreased rapidly with slight hypsochromic shifts (555.3 nm) in Fig. 9(b); no new absorption

bands appeared, even in the ultraviolet region ($\lambda > 200 \text{ nm}$), indicating the potential formation of a series of *N*-demethylated intermediates and cleavage of the conjugated chromophore of the CV dye. Further irradiation decreased the absorption band at 555.3 nm; however, no further wavelength shift was observed. Thus, it was inferred that the band at 555.3 nm was that of the full *N*-demethylated product of the CV dye.

In Fig. 10, the lowest relative CL intensity of BiOBr , $\text{Bi}_3\text{O}_4\text{Br}$, and $\text{Bi}_{12}\text{O}_{17}\text{Br}_2$ suggested that it had the lowest recombination rate of electron-hole pairs, which resulted in the highest photocatalytic activity of $\text{Bi}_3\text{O}_4\text{Br}$, as shown in Figure 7. Therefore, it was believed that the CV degradation was initiated not only by a photocatalytic process but also by a photosensitization process.

The durability of BiOBr (Fig. 11(a)), $\text{Bi}_3\text{O}_4\text{Br}$ (Fig. 11(b)), and $\text{Bi}_{12}\text{O}_{17}\text{Br}_2$ (Fig. 11(c)) was evaluated by recycling the used catalyst. After each cycle, the catalyst was collected by centrifugation. No apparent loss was observed in the photocatalytic activity when CV was removed in the third cycle; even during the fifth run, the decline in the photocatalytic activity was 7% (Fig. 11). The used BiOBr , $\text{Bi}_3\text{O}_4\text{Br}$, and $\text{Bi}_{12}\text{O}_{17}\text{Br}_2$ were also examined by XRD and no detectable difference was observed between the as-prepared and used samples (Fig. 12); hence, BiOBr , $\text{Bi}_3\text{O}_4\text{Br}$, and $\text{Bi}_{12}\text{O}_{17}\text{Br}_2$ presented good photostability. It indicated that the new samples prepared were highly stable and did not photocorrode during the photocatalysis of the model pollutant molecules, which was principal for its application.

On the basis of all the above experimental results, these nanosheet and/or nanoplate structures (Figs. 2–3 and Figs. S5–S8) could provide efficient transport paths for reactants and more active sites for the photocatalytic reaction. In Fig. 10, the lowest relative CL intensity of BiOBr , $\text{Bi}_3\text{O}_4\text{Br}$, and $\text{Bi}_{12}\text{O}_{17}\text{Br}_2$ suggested that it had the lowest recombination rate of electron-hole pairs. The structures were also favorable to efficient photo-energy harvesting and introducing the separation of electron-hole pairs, thus promoting the photocatalytic activity. From Table 4, $\text{Bi}_3\text{O}_4\text{Br}$ had larger BET and pore volume in all samples prepared. Thus, the large BET and pore volume of $\text{Bi}_3\text{O}_4\text{Br}$ might play a role in enhancing the photocatalytic activity.

4. Conclusions

In a summary, the pH of a reaction is generally accepted to have great influence on determining the composition and morphologies of the final products. Control experiments have been conducted to investigate the influence of pH on the reaction. The increased photocatalytic activities of BiOBr , $\text{Bi}_3\text{O}_4\text{Br}$, and $\text{Bi}_{12}\text{O}_{17}\text{Br}_2$ could be attributed to the formation of the nanosheets and nanoplates effectively suppressing the recombination of the photoinduced electron-hole pairs. The large surface areas and pore volume, hierarchical structure and modified band structure in all contribute to the dramatic activity enhancement. The activity of $\text{Bi}_3\text{O}_4\text{Br}$ is higher than those of BiOBr , Bi_2WO_6 , P25-TiO₂, and $\text{Bi}_{12}\text{O}_{17}\text{Br}_2$. The excellent activity and photostability reveal that bismuth oxybromides are a promising visible-light-responsive photocatalyst. The research results could not only provide new insights into the pH effect on synthesis of hierarchical nanosheets with enhanced properties, but also could provide an effective approach for the design of high performance visible-light-driven photocatalysts for environmental applications.

Acknowledgment

This research was supported by the National Science Council of the Republic of China (NSC-101-2113-M-142-001-MY3).

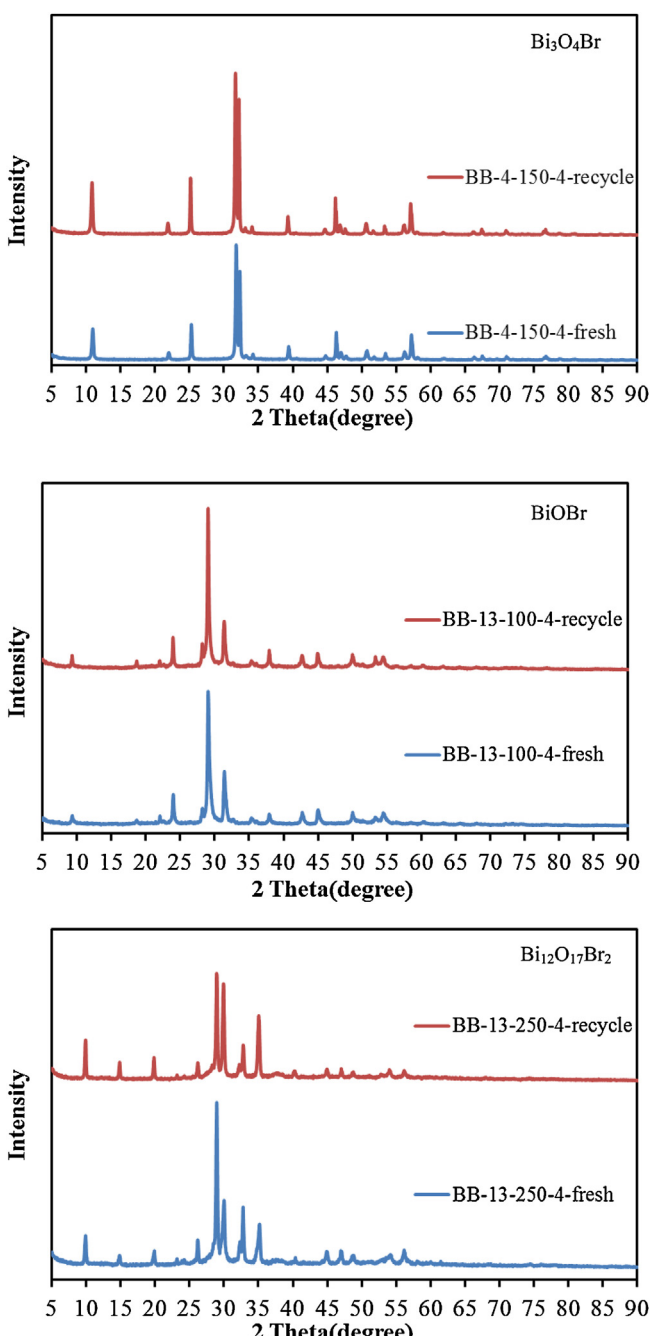


Fig. 12. XRD patterns acquired before and after in the photocatalytic degradation of CV in the presence of (a) $\text{Bi}_3\text{O}_4\text{Br}$, (b) BiOBr , (c) $\text{Bi}_{12}\text{O}_{17}\text{Br}_2$.

Appendix A. Supplementary data

Supplementary material related to this article can be found, in the online version, at <http://dx.doi.org/10.1016/j.jtice.2014.04.001>.

References

- [1] Shannon MA, Bohn PW, Elimelech M, Georgiadis JG, Marinas BJ, Mayes AM. Science and technology for water purification in the coming decades. *Nature* 2008;452:301–10.
- [2] Khan SUM, Al-Shahry M, Ingler WB. Efficient photochemical water splitting by a chemically modified *n*-TiO₂. *Science* 2002;297:2243–5.
- [3] Liao YHB, Wang JX, Lin JS, Chung WH, Lin WY, Chen CC. Synthesis, photocatalytic activities and degradation mechanism of Bi₂WO₆ toward crystal violet dye. *Catal Today* 2011;174:148–59.
- [4] Ren J, Wang W, Shang M, Sun S, Gao E. Heterostructured bismuth molybdate composite: preparation and improved photocatalytic activity under visible-light irradiation. *ACS Appl Mater Interfaces* 2011;3:2529–33.
- [5] Wang D, Li R, Zhu J, Shi J, Han J, Zong X, Li C. Photocatalytic water oxidation on BiVO₄ with the electrocatalyst as an oxidation cocatalyst: essential relations between electrocatalyst and photocatalyst. *J Phys Chem C* 2012;116:5082–9.
- [6] Casbeer E, Sharma VK, Li XZ. Synthesis and photocatalytic activity of ferrites under visible light: a review. *Sep Purif Technol* 2012;87:1–14.
- [7] Kudo A, Omori K, Kato H. A novel aqueous process for preparation of crystal form-controlled and highly crystalline BiVO₄ Powder from layered vanadates at room temperature and its photocatalytic and photophysical properties. *J Am Chem Soc* 1999;121:11459–67.
- [8] Xu J, Meng W, Zhang Y, Li L, Guo C. Photocatalytic degradation of tetrabromobiphenol A by mesoporous BiOBr: efficacy, products and pathway. *Appl Catal B: Environ* 2011;107:355–62.
- [9] Huo Y, Zhang J, Miao M, Jin Y. Solvothermal synthesis of flower-like BiOBr microspheres with highly visible-light photocatalytic performances. *Appl Catal B: Environ* 2012;111–112:334–41.
- [10] Xu J, Li L, Guo C, Zhang Y, Wang S. Removal of benzotriazole from solution by BiOBr photocatalysis under simulated solar irradiation. *Chem Eng J* 2013;221:230–7.
- [11] Xia J, Yin S, Li H, Xu H, Xu L, Xu Y. Improved visible light photocatalytic activity of sphere-like BiOBr hollow and porous structures synthesized via a reactable ionic liquid. *Dalton Trans* 2011;40:5249–58.
- [12] Fang Y, Huang Y, Yang J, Wang P, Cheng G. Unique ability of BiOBr to decarboxylate *D*-Glu and *D*-MeAsp in the photocatalytic degradation of microcystin-LR in water. *Environ Sci Technol* 2011;45:1593–600.
- [13] Deng H, Wang J, Peng Q, Wang X, Li Y. Controlled hydrothermal synthesis of bismuth oxyhalide nanobelts and nanotubes. *Chem Eur J* 2005;11:6519–24.
- [14] Cheng H, Huang B, Wang Z, Qin X, Zhang X, Dai Y. One-pot miniemulsion-mediated route to BiOBr hollow microspheres with highly efficient photocatalytic activity. *Chem Eur J* 2011;17:8039–43.
- [15] Shang M, Wang W, Zhang L. Preparation of BiOBr lamellar structure with high photocatalytic activity by CTAB as Br source and template. *J Hazard Mater* 2009;167:803–9.
- [16] Huang WL, Zhu Q. DFT calculations on the electronic structures of BiOX (X = F, Cl, Br, I) photocatalysts with and without semicore Bi 5d states. *J Comput Chem* 2009;30:183–90.
- [17] Deng ZT, Chen D, Peng B, Tang FQ. From bulk metal Bi to two-dimensional well-crystallized BiOX (X = Cl, Br) micro- and nanostructures: synthesis and characterization. *Cryst Growth Des* 2008;8:2995–3003.
- [18] Wang J, Li Y. Synthesis of single-crystalline nanobelts of ternary bismuth oxide bromide with different compositions. *Chem Commun* 2003;2320–1.
- [19] Keller E, Kraemer V. Bi₅O₇Br and its structural relation to α -Bi₅O₇. *Acta Cryst* 2007;C63:1109–11.
- [20] Wang J, Yu Y, Zhang L. Highly efficient photocatalytic removal of sodium pentachlorophenate with Bi₃O₄Br under visible light. *Appl Catal B: Environ* 2013;136–137:112–21.
- [21] Eggenweiler U, Keller E, Kramer V. Redetermination of the crystal structures of the 'Arppe compound' Bi₂₄O₃₁Cl₁₀ and the isomorphous Bi₂₄O₃₁Br₁₀. *Acta Cryst* 2000;B56:431–7.
- [22] Rittner P, Oppermann H. Calorimetry of bismuth oxyhalides. II. Bismuth oxide bromides. *Z Anorg Allg Chem* 1992;615:123–6.
- [23] Xiao X, Hu R, Liu C, Xing C, Zuo X, Nan J, Wang L. Facile microwave synthesis of novel hierarchical Bi₂₄O₃₁Br₁₀ nanoflakes with excellent visible light photocatalytic performance for the degradation of tetracycline hydrochloride. *Chem Eng J* 2013;225:790–7.
- [24] Keller E, Ketterer J, Kramer V. Crystal structure and twinning of Bi₄O₅Br₂. *Z Kristallogr* 2001;216:595–9.
- [25] Yu C, Zhou W, Yu J, Cao F, Li X. Thermal stability, microstructure and photocatalytic activity of the bismuth oxybromide photocatalyst. *Chin J Chem* 2012;30:721–6.
- [26] Xiao X, Liu C, Hu R, Zuo X, Nan J, Li L, Wang L. Oxygen-rich bismuth oxyhalides: generalized one-pot synthesis, band structures and visible-light photocatalytic properties. *J Mater Chem* 2012;22:22840–43.
- [27] Jovalekic C, Pavlovic M, Osmokrovic P, Atanasoska L. X-ray photoelectron spectroscopy study of Bi₄Ti₃O₁₂ ferroelectric ceramics. *Appl Phys Lett* 1998;72:1051–3.
- [28] Liao YH, Wang JX, Lin JS, Chung WH, Lin WY, Chen CC. Synthesis photocatalytic activities and degradation mechanism of Bi₂WO₆ toward crystal violet dye. *Catal Today* 2011;174:148–59.
- [29] Lee WW, Lin J, Chang J, Chen J, Cheng M, Chen CC. Photodegradation of CV over nanocrystalline bismuth tungstate prepared by hydrothermal synthesis. *J Mol Catal A: Chem* 2012;361–362:80–90.
- [30] Dong F, Sun Y, Fu M, Wu Z, Lee SC. Room temperature synthesis and highly enhanced visible light photocatalytic activity of porous BiOI/BiOCl composites nanoplates microflowers. *J Hazard Mater* 2012;219–220:26–34.
- [31] Sing KSW, Everett DH, Haul RAW, Moscou L, Pierotti RA, Rouquerol J, Siemieniewska T. Reporting physisorption data for gas/solid systems. *Pure Appl Chem* 1985;57:603–19.
- [32] Yu JG, Su YR, Cheng B. Template-free fabrication and enhanced photocatalytic activity of hierarchically macro/mesoporous titania. *Adv Funct Mater* 2007;17:1984–90.
- [33] Herrmann JM, Tahiri H, Ait-Ichou Y, Lassaletta G, Gonzalez-Elipe AR, Fernandez A. Characterization and photocatalytic activity in aqueous medium of TiO₂ and Ag-TiO₂ coatings on quartz. *Appl Catal B: Environ* 1997;13:219–28.